The Astrophysical Journal, 929:31 (9pp), 2022 April 10 https://doi.org/10.3847/1538-4357/ac59b1

Relativistic Alfvén Waves Entering Charge-starvation in the Magnetospheres of Neutron Stars

Alexander Y. Chen[1], Yajie Yuan[2], Andrei M. Beloborodov[3,4], and Xinyu Li[5,6]
[1] JILA, University of Colorado Boulder, 440 UCB, Boulder, CO 80309, USA; yuran.chen@colorado.edu
[2] Center for Computational Astrophysics, Flatiron Institute, 162 Fifth Avenue, New York, NY 10010, USA
[3] Physics Department and Columbia Astrophysics Laboratory, Columbia University, 538 West 120th Street New York, NY 10027, USA
[4] Max Planck Institute for Astrophysics, Karl-Schwarzschild-Str. 1, D-85741, Garching, Germany
[5] Canadian Institute for Theoretical Astrophysics, 60 St George St, Toronto, ON M5R 2M8, Canada
[6] Perimeter Institute for Theoretical Physics, 31 Caroline Street North, Waterloo, Ontario, N2L 2Y5, Canada
Received 2020 October 29; revised 2022 January 28; accepted 2022 February 28; published 2022 April 11

Abstract

Instabilities in a neutron star can generate Alfvén waves in its magnetosphere. Propagation along the curved magnetic field lines strongly shears the wave, boosting its electric current j_A. We derive an analytic expression for the evolution of the wavevector $\boldsymbol{k}$ and the growth of j_A. In the strongly sheared regime, j_A may exceed the maximum current j_0 that can be supported by the background $e^{\pm}$ plasma. We investigate these *charge-starved* waves, first using a simplified two-fluid analytic model, then with first-principles kinetic simulations. We find that the Alfvén wave is able to propagate successfully even when $\kappa \equiv j_A/j_0 \gg 1$. It sustains j_A by compressing and advecting the plasma along the magnetic field lines with an increasing Lorentz factor, $\gamma \gtrsim \kappa^{1/2}$. The simulations show how plasma instabilities lead to gradual dissipation of the wave energy. Our results suggest that an extremely high charge-starvation parameter $\kappa \gtrsim 10^4$ may be required in order for this mechanism to power the observed fast radio bursts (FRBs) from SGR 1935+2154. However, cosmological FRBs with much higher luminosities are unlikely to be a result of charge-starvation.

Unified Astronomy Thesaurus concepts: Plasma physics (2089); Neutron stars (1108); Radio bursts (1339)

1. Introduction

Young and active neutron stars can experience quakes that are capable of launching low-frequency (kHz) Alfvén waves into the star's magnetosphere (Blaes et al. 1989). This process can power X-ray bursts from magnetars (Duncan & Thompson 1992). Quakes have also been associated with glitches in the rotational frequencies of young radio pulsars (e.g., Ruderman 1976), and the quake excitation of magnetospheric Alfvén waves was invoked to explain the chocking of the radio signal from the Vela pulsar during a glitch (Palfreyman et al. 2018; Bransgrove et al. 2020). Alfvén waves may also be involved in the production of the fast radio burst (FRB) detected recently from the galactic magnetar SGR 1935+2154 (Bochenek et al. 2020; CHIME/FRB Collaboration et al. 2020; Mereghetti et al. 2020).

The group velocity of an Alfvén wave in the magnetosphere of a neutron star is near the speed of light c, and it is directed along the magnetic field $\boldsymbol{B}_0$. Propagation along the curved magnetic field lines leads to the growth of $k_\perp$, the wavenumber perpendicular to $\boldsymbol{B}_0$ (Bransgrove et al. 2020). This process can strongly enhance the electric current in the Alfvén wave $j_A \sim (c/4\pi)k_\perp B_w$, where B_w is the wave amplitude.

The maximum current that can be supported by a plasma with density n_0 is en_{0c}, and it is convenient to define the dimensionless parameter

$$\kappa \equiv \frac{j_A}{j_0}, \qquad j_0 = en_0 c. \tag{1}$$

The regime of $\kappa > 1$ is often called *charge-starved*. Charge-starvation has long been invoked as a possible dissipation mechanism of magnetospheric waves (Blaes et al. 1989; Thompson & Blaes 1998). Recently, it has been proposed that waves entering the regime of $\kappa > 1$ will develop a strong electric field $E_\parallel$ (parallel to $\boldsymbol{B}_0$) and dissipate a large fraction of the wave energy, possibly accompanied by strong plasma bunching and coherent radio emission, which was suggested as a potential mechanism for FRB emission (Kumar et al. 2017; Kumar & Bošnjak 2020; Lu et al. 2020).

In this paper, we examine the behavior of charge-starved Alfvén waves. In particular, we wish to know what $E_\parallel$ is induced, how much of the wave energy is dissipated, what plasma instabilities will arise, and what is the resulting particle distribution. We begin with a discussion of how an Alfvén-wave packet can become charge-starved as it propagates in the magnetosphere of a neutron star (Section 2). Then we investigate what happens with the wave as it enters the regime of $\kappa > 1$. We first use a simplified analytical model (Section 3), then perform direct kinetic simulations of the plasma dynamics in the wave (Section 4).

2. Propagation and Shearing of an Alfvén-wave Packet

Consider an Alfvén-wave packet launched into the magnetosphere by a shear motion of the neutron star crust. Let B_w be the wave amplitude and $\ell_\perp$ be the perpendicular size of the packet. The initial $\ell_\perp$ equals the size of the sheared region of the stellar surface, which determines the current density in the packet $j_A \sim (c/4\pi)B_w/\ell_\perp$ that flows along the background magnetic field $\boldsymbol{B}_0$. Small amplitude waves with $B_w \ll B_0$ will propagate along the magnetic field lines without disrupting the structure of the magnetosphere. Below we examine two main effects that

will affect the evolution of j_A as the wave packet propagates away from the star.

First, the divergence of the dipole field lines will increase $\ell_\perp$ and decrease B_w. The distance between magnetic flux surfaces increases with radius r as $\ell_\perp \propto r^{3/2}$ while $B_w \propto r^{-3/2}$. This effect leads to a scaling of $j_A \propto r^{-3}$. Incidentally, the Goldreich–Julian charge density ρ_{GJ} in a rotating dipole magnetosphere also decreases as r^{-3} (Goldreich & Julian 1969). This led Kumar & Bošnjak (2020) to suggest that, in a magnetosphere with plasma density $n = \mathcal{M}\rho_{GJ}/e$, the Alfvén wave can become charge-starved if the multiplicity $\mathcal{M}$ decreases with the radius. On closed field lines, when the wave packet reaches the magnetic equator and turns back to the star, it follows the converging field lines, and $\ell_\perp$ decreases again. If the divergence/convergence of the magnetic flux surfaces were the only effect, j_A would come to its original value when reaching the stellar surface in the opposite hemisphere.

However, there is a second effect that can enhance the perpendicular gradient of the Alfvén-wave packet, hence increasing j_A, especially on closed field lines. Different dipole field lines have different lengths, and the parts of the packet propagating along the longer field lines lag behind, leading to a strong shear of the packet. Bransgrove et al. (2020) described this effect as "de-phasing," and studied the evolution of j_A as the wave keeps bouncing in the closed magnetosphere. Here we use a different approach to compute the evolution of $k_\perp$ within a single pass in the magnetosphere.

A dipole magnetic field line is parameterized by $r = r_m \sin^2\theta$, where r_m is the radius where it crosses the magnetic equator ($\theta = \pi/2$). The field line starts at the stellar surface (radius $r_\star$) at polar angle θ_0 related to r_m by $\sin^2\theta_0 = r_\star/r_m$. It is convenient to use variable $\mu = \cos\theta$, which varies along the closed field line between μ_0 and $-\mu_0$. Starting from the northern footpoint μ_0, one can integrate the length along the dipole field line to a given point μ,

$$\begin{aligned} s(r_m, \mu) &= r_m \int_\mu^{\mu_0} \sqrt{3\mu_1^2 + 1}\, d\mu_1 \\ &= r_m[F(\mu_0) - F(\mu)], \end{aligned} \tag{2}$$

where

$$F(\mu) = \frac{1}{2}\mu\sqrt{1+3\mu^2} + \frac{\sinh^{-1}(\sqrt{3}\,\mu)}{2\sqrt{3}}. \tag{3}$$

Note that $\mu_0 = (1 - r_\star/r_m)^{1/2}$, so $F(\mu_0)$ is a function of r_m.

Let us now consider an Alfvén wave with the frequency ω launched from the stellar surface in the northern hemisphere. The wave at $t > 0$ is described by $B_w(r/r_*)^{-3/2}\exp[i\Phi(t, \boldsymbol{r})]$, where

$$\Phi(t, \boldsymbol{r}) = \Phi_0(r_m) - \omega t + k_\parallel s(\boldsymbol{r}), \qquad k_\parallel = \frac{\omega}{c}. \tag{4}$$

As long as $c/\omega \ll r_*$ and the initial $\ell_\perp \ll r_*$, the wavevector is $\boldsymbol{k} = \nabla\Phi = \nabla\Phi_0 + (\omega/c)\nabla s$. The first term is the contribution to $\boldsymbol{k}$ from the initial profile of the perturbation. The evolution of $\nabla_\perp\Phi_0$ follows the divergence of the field lines, and is essentially the first effect we discussed above. We are interested in the evolution of $k_\perp$ due to the second term, $k_\perp = (\omega/c)\nabla_\perp s$.

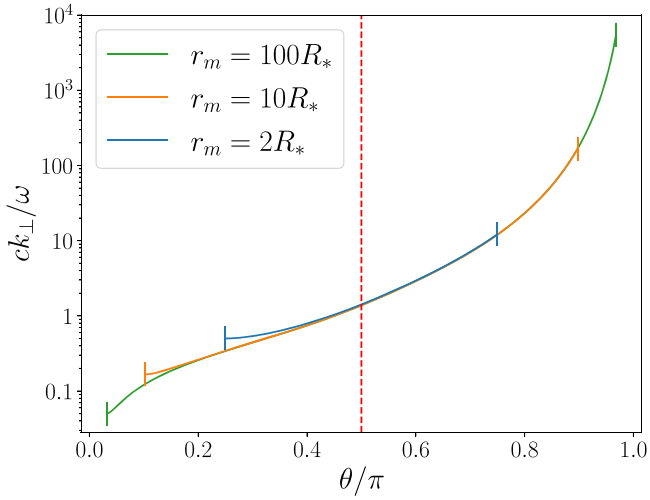

Figure 1. The evolution of $k_\perp$ on field lines of different r_m. The vertical markers indicate the footpoints of the magnetospheric field line on the star. The red dashed vertical line shows the magnetic equator $\theta = \pi/2$.

To evaluate $\nabla_\perp s$, it is convenient to introduce the dipole coordinates following Swisdak (2006):

$$\eta = \frac{r}{\sin^2\theta} = r_m, \quad \chi = \frac{\cos\theta}{r^2} = \frac{\mu}{r^2}. \tag{5}$$

The η-coordinate coincides with r_m, and uniquely labels the field lines, while the χ-coordinate varies along a single field line. This is an orthogonal coordinate system with metric elements:

$$h_\eta = \sqrt{g_{\eta\eta}} = \frac{\sin^3\theta}{\sqrt{1+3\mu^2}}, \quad h_\chi = \sqrt{g_{\chi\chi}} = \frac{r^3}{\sqrt{1+3\mu^2}}. \tag{6}$$

The metric coefficient h_η quantifies the distance between the dipole flux surfaces. The perpendicular derivative is simply given by the following:

$$\frac{ck_\perp}{\omega} = \nabla_\perp s = \frac{1}{h_\eta}\frac{\partial s}{\partial \eta}\bigg|_\chi, \tag{7}$$

which can be evaluated to be the following:

$$\begin{aligned} \frac{ck_\perp}{\omega} = \frac{\sqrt{1+3\mu^2}}{\sin^3\theta}\Bigg([F(\mu_0) - F(\mu)] \\ + \frac{\sqrt{1+3\mu_0^2}}{2\mu_0}\frac{r_\star}{r_m} - 2\frac{\mu\sin^2\theta}{\sqrt{1+3\mu^2}}\Bigg). \end{aligned} \tag{8}$$

The variation of $k_\perp$ along a given field line is shown in Figure 1. For extended field lines, $r_m \gg r_*$, $k_\perp$ can grow to very large values in the southern hemisphere. This is a combination of two effects. The cumulative path difference $\partial s/\partial\eta$ grows fastest near the equator, which leads to $k_\perp \sim \omega/c$. Then, due to the field line convergence in the southern hemisphere, the existing $k_\perp$ is increased by a factor of $1/h_\eta \sim (r_m/r_*)^{3/2}$ when the wave reaches the southern footpoint. After N consecutive bounces, the wave will accumulate a total $ck_\perp \propto N\omega/h_\eta$, consistent with the result of Bransgrove et al. (2020; their Equation (38) used the approximation $\nabla_\perp \sim r^{-1}\partial_\theta$, which is valid for θ away from the equatorial plane). The reflection coefficient of Alfvén waves at the stellar surface was calculated

by Li & Beloborodov (2015) to be $\mathcal{R} \sim 0.9$, so most of the wave energy is reflected at each bounce, and $k_\perp$ keeps growing as the waves bounce along the closed magnetic field lines.

The evolution of $ck_\perp/\omega$ results in the Alfvén wave front becoming increasingly oblique with respect to the background field $\boldsymbol{B}_0$. The angle ψ between the wavevector $\boldsymbol{k}$ and $\boldsymbol{B}_0$ grows as $\tan\psi = k_\perp/k_\parallel = ck_\perp/\omega$. The dimensionless parameter κ grows as follows:

$$\kappa = \frac{j_A}{en_0c} \sim \frac{\omega_B \omega \tan\psi}{\omega_p^2}\frac{B_w}{B_0}, \tag{9}$$

where $\omega_p = \sqrt{4\pi e^2 n_0/m_e}$ is the background plasma frequency, and $\omega_B = eB_0/m_ec$ is the gyro-frequency of electrons in the background magnetic field. Due to the ever-growing $\tan\psi$, the effect of wave shearing can eventually lead to charge-starvation, $\kappa > 1$, even for waves of modest amplitudes.

3. Plasma Dynamics in the Wave: Two-fluid Model

3.1. Problem Setup

As a first step toward understanding charge-starved Alfvén waves, we examine a simple two-fluid model of plasma motion in a plane wave propagating into a uniform background. The uniform approximation is reasonable for sufficiently short waves. We take the background to be a cold neutral $e^\pm$ plasma with density $n_+ = n_- = n_0 = \text{const}$ immersed in a uniform magnetic field $\boldsymbol{B}_0$. A gradual change of κ may then be treated as an adiabatic effect on the quasi-steady plane wave.

We are interested in the highly magnetized regime with $\sigma \equiv B_0^2/4\pi n_0 m_e c^2 \gg 1$, so that the propagation speed of the wave along $\boldsymbol{B}_0$ nearly equals c. The electromagnetic field of a steadily propagating wave is then only a function of $t - s/c$, where the s-coordinate runs along $\boldsymbol{B}_0$. Let the x-axis be along the wavevector $\boldsymbol{k}$; the wave magnetic field $\boldsymbol{B}$ depends on

$$\xi = t - \frac{s}{c} = t - \frac{x}{c\cos\psi}. \tag{10}$$

The propagation speed along x is $V_x = c\cos\psi$. The wave electric field $\boldsymbol{E}$ is related to the magnetic field $\boldsymbol{B}$ by

$$\boldsymbol{E}(\xi) = \boldsymbol{B}(\xi) \times \frac{\boldsymbol{B}_0}{B_0}. \tag{11}$$

The wave fields $\boldsymbol{B}$ and $\boldsymbol{E}$ are both perpendicular to the background field. The electric current density in the wave is parallel to $\boldsymbol{B}_0$, and its value is

$$j_A(\xi) = \frac{\tan\psi}{4\pi}\frac{dB}{d\xi}. \tag{12}$$

The charge density in the wave, $\rho = \nabla\cdot\boldsymbol{E}/4\pi$ satisfies the relation

$$c\rho(\xi) = j_A(\xi). \tag{13}$$

The above description gives an exact MHD solution in the force-free limit $\sigma \to \infty$ with no charge-starvation. It relies on the implicit assumption that there is always enough plasma to conduct the required electric current j_A. We will next examine the dynamics of the $e^\pm$ particles for any given background plasma density n_0, especially in the regime $\kappa > 1$, when the assumption of a copious plasma supply may not be valid.

The characteristic gyro-frequency ω_B in the neutron star magnetosphere is many orders of magnitude greater than ω. Therefore, $e^\pm$ particles in the wave move with velocities $\boldsymbol{v}$ along the magnetic field lines, like beads on a wire. Only $E_\parallel$ is relevant for their dynamics. For small amplitude waves $B_w \ll B_0$, the field lines are bent only by a small angle, and $v_\parallel = \boldsymbol{v}\cdot\boldsymbol{B}_0/B_0 + \mathcal{O}(B_w^2/B_0^2)$. Therefore we approximate the particle motion as parallel to $\boldsymbol{B}_0$.

In order to conduct the required electric current, an $E_\parallel$ will be induced to accelerate the electrons and positrons in opposite directions, creating two plasma streams.

3.2. Two-fluid Model

We first examine a simple model assuming that the $e^\pm$ streams remain cold, neglecting any possible instabilities that may arise. This "two-fluid" model captures some basic features of the plasma dynamics in the wave. The parallel electric field regulating the velocities of the $e^\pm$ streams is nondissipative in the two-fluid model, as the particles will come to rest behind the wave.

The two cold fluids are described by their densities $n_\pm$ and velocities $v_\pm$. Both are functions of ξ in a steadily propagating wave. Their values in the background plasma, $n_\pm = n_0$ and $v_\pm = 0$, give the boundary conditions ahead of the wave for the profiles $n_\pm(\xi)$ and $v_\pm(\xi)$. The density and velocity of each stream satisfies the continuity equation $\partial_t n_\pm + \partial_x(n_\pm v_{\pm,x}) = 0$, where $v_{\pm,x} = v_\pm\cos\psi$. This gives

$$\frac{dn_\pm}{d\xi} - \frac{d}{d\xi}(n_\pm\beta_\pm) = 0, \tag{14}$$

where $\beta_\pm = v_\pm/c$. One then finds $(1-\beta_\pm)dn_\pm = n_\pm d\beta_\pm$ and

$$n_\pm(\xi) = \frac{n_0}{1-\beta_\pm(\xi)}, \tag{15}$$

where we used the boundary condition ahead of the wave: $n_\pm = n_0$ when $v_\pm = 0$. In the two-fluid picture, the continuity equation automatically implies the relation $j = \rho c$, where $j = e(n_+v_+ - n_-v_-)$ and $\rho = e(n_+ - n_-)$.

The fluid velocities are related to $\kappa = j_A/en_0c$ by

$$\frac{1}{1-\beta_+} - \frac{1}{1-\beta_-} = \kappa(\xi). \tag{16}$$

In a successfully propagating Alfvén wave, the plasma motion must sustain $j = j_A$ given in Equation (12), which determines $\kappa(\xi)$. Our goal is to find $\beta_\pm(\xi)$ under a given $\kappa(\xi)$, and then check what happens in the charge-starvation regime of $\kappa > 1$.

Particles are governed by the equation of motion $dp_\pm/dt = \pm eE_\parallel$, where $p_\pm = \gamma_\pm m_e v_\pm$, $\gamma_\pm = (1-\beta_\pm^2)^{-1/2}$, and $d/dt = \partial_t + v_\pm d/ds = (1-\beta_\pm)d/d\xi$. This equation gives

$$\frac{dq_\pm}{d\xi} = \pm\frac{eE_\parallel}{m_ec}, \qquad q_\pm \equiv \gamma_\pm(1-\beta_\pm). \tag{17}$$

It implies $d(q_+ + q_-)/d\xi = 0$. Then using the boundary condition $q_+ = q_- = 1$ ahead of the wave, we obtain

$$q_+ + q_- = 2. \tag{18}$$

Rewriting Equation (16) in terms of $q_\pm$,

$$\frac{1}{q_+^2} - \frac{1}{q_-^2} = 2\kappa(\xi), \tag{19}$$

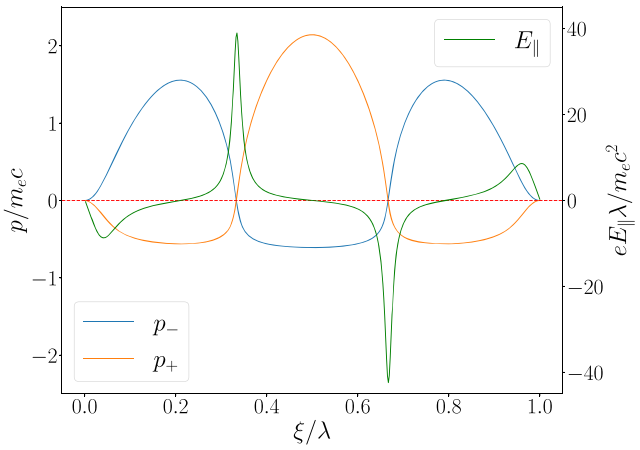

Figure 2. The momentum profile $p_\pm(\xi)$ of the electron (blue) and positron (orange) streams in the two-fluid model, for the wave profile given in Equation (21). The corresponding $E_\parallel(\xi)$ is shown by the green curve. The maximum κ in this example is 10, reached at the center of the wave profile.

we obtain two equations for $q_\pm$, which can be easily solved for any given $\kappa(\xi)$. Once $q_\pm(\xi)$ are found, we also obtain $eE_\parallel = m_e c\, dq_+/d\xi$.

A well-behaved solution to Equations (18) and (19) exists for both $|\kappa| < 1$ and $|\kappa| > 1$. In particular, consider $\kappa \gg 1$, the strongly *charge-starved* regime with $j > 0$. Then the solution is $q_+^{-2} \approx 2\kappa \gg q_-^{-2} \approx 1/4$. Using the relation $q^{-1} = \gamma(1+\beta)$, we find

$$\gamma_+ \approx \left(\frac{\kappa}{2}\right)^{1/2}, \quad \gamma_- \approx \frac{5}{4} \qquad (\kappa \gg 1). \tag{20}$$

Figure 2 shows the solution for $p_\pm(\xi)$, and the corresponding $E_\parallel(\xi)$, for a plane wave with the following profile:

$$\frac{B}{B_w} = \begin{cases} \frac{8}{3\sqrt{3}} \sin\left(2\pi\frac{\xi}{\lambda}\right) \sin^2\left(\pi\frac{\xi}{\lambda}\right), & 0 < \xi < \lambda \\ 0, & \text{otherwise.} \end{cases} \tag{21}$$

This profile describes an isolated sine pulse, with the additional factor of $\sin^2(\pi\xi/\lambda)$ introduced to make the derivative $dB/d\xi$ smoothly vanish at the boundaries of the pulse $\xi = 0$, λ. In our example, $\kappa(\xi)$ reaches the maximum $\kappa_w = 10$ at $\xi = 0.5\lambda$.

The wave achieves the required j and ρ by inducing $E_\parallel$ that sweeps the $e^\pm$ particles along $\boldsymbol{B}_0$. This sweeping compresses the two fluids by the factors of $(1-\beta_\pm)^{-1}$ (Equation (15)). In the regime of $\kappa \gg 1$, the compression factor is large for e^+, $(1-\beta_+)^{-1} \approx 2\gamma_+^2$. Developing $\gamma_+ \approx (\kappa/2)^{1/2}$ is sufficient to enhance the local density of e^+ by the factor of κ and thus achieve ρ and j required by the wave. Charges of the opposite sign do not suffer from this compression, and they are only mildly accelerated to $\gamma_- \approx 5/4$, or $\beta_- \approx 0.6$. Particles move through the wave with the relative speed $c - v \approx c/2\gamma^2$ when $\gamma \gg 1$; therefore it takes time $t_{\rm res} \sim \kappa\lambda/c$ for the plasma to cross the wave.

It is convenient to define

$$n_w = \frac{j_{\rm A}}{ec}. \tag{22}$$

In the charge-starved regime $\kappa \gg 1$, the wave carries the density $n \approx n_w$, and the electromagnetic energy available per particle is described by

$$\sigma_w = \frac{B_w^2}{4\pi n_w m_e c^2}. \tag{23}$$

The wave propagation is weakly affected by charge-starvation as long as $\gamma_+ \approx (\kappa/2)^{1/2} \ll \sigma_w$. Otherwise the plasma kinetic energy will become comparable to the field energy, leading to significant deviations of $\boldsymbol{E}(\xi)$ and $\boldsymbol{B}(\xi)$ from the force-free solution.

In neutron star magnetospheres, the plasma frequency ω_p is much higher than the frequencies of Alfvén waves launched by crustal motion. This implies that the two-fluid model is deficient, because this configuration is unstable to the two-stream instability on the short plasma timescale $\sim\omega_p^{-1}$. In particular, consider the vicinity of a maximum of $p_\pm$ in Figure 2, where the two-fluid model gives $E_\parallel \approx 0$. Since the parameters of the $e^\pm$ streams are varying slowly compared to the plasma scale, $\omega \ll \omega_p$, one can use the standard linear instability analysis (e.g., Melrose 1986) to find that the most unstable mode is near $k \sim \omega_p/c$ with the growth rate $\Gamma \sim \omega_p$. The instability will heat the plasma streams and mix them in the phase space. It is difficult to analytically predict the consequences of the nonlinear saturation of the instability. Therefore, we employ direct kinetic plasma simulations to find a self-consistent solution.

4. Numerical Simulations

4.1. Simulation Setup

We set up a series of particle-in-cell (PIC) simulations using our own GPU-based PIC code *Aperture*.[7] We use a two-dimensional, elongated Cartesian box with periodic boundary conditions in the y direction. An Alfvén wave is initialized at the left end of the box with the profile described by Equation (21), with magnitude B_w and wave $\boldsymbol{B}$ pointing in the z direction. The wave electric field is initialized using Equation (11). The background magnetic field $\boldsymbol{B}_0$ is inclined with respect to the x-axis by an angle ψ. In our simulations, $\cos\psi = \hat{\boldsymbol{B}}_0 \cdot \hat{\boldsymbol{x}} = 0.15$. As the wave propagates along $\boldsymbol{B}_0$, it will move in the box along the x direction. The effective length of propagation is much longer than the box length due to the inclination of the background field. A damping layer is placed at the end of the box $x = L_x$ to prevent the reflection of any plasma waves.

We start with a small amplitude wave, with $B_w/B_0 = 0.1$. Inside the wave packet, we initialize a pair plasma that satisfies $\rho = j_{\rm A}/c$ and $j = j_{\rm A}$ with a small initial multiplicity, $n_+ + n_- = 3j_{\rm A}/ec$. The space outside of the wave packet is filled with a low-density neutral plasma with $n_+ = n_- = n_0$. We typically have 5–10 particles per cell corresponding to n_0. Depending on the value of κ, the number of particles per cell in the wave is often much larger. The characteristic plasma skin depth c/ω_p in the wave is set by $j_{\rm A}/ec$, and is typically $\sim 1/200$ of the wavelength in the x direction, λ_x. The box size is $L_x = 5\lambda_x = 10L_y$, and has a total resolution 5120×512. This translates to $\sim$5 cells per plasma skin depth. Outside the wave packet, where plasma density $n_0 \ll j_{\rm A}/ec$, the plasma skin depth is resolved with many more cells.

This problem has two dimensionless parameters, κ and σ_w. In the following discussion, we refer to κ as its maximum value

[7] https://github.com/fizban007/Aperture4

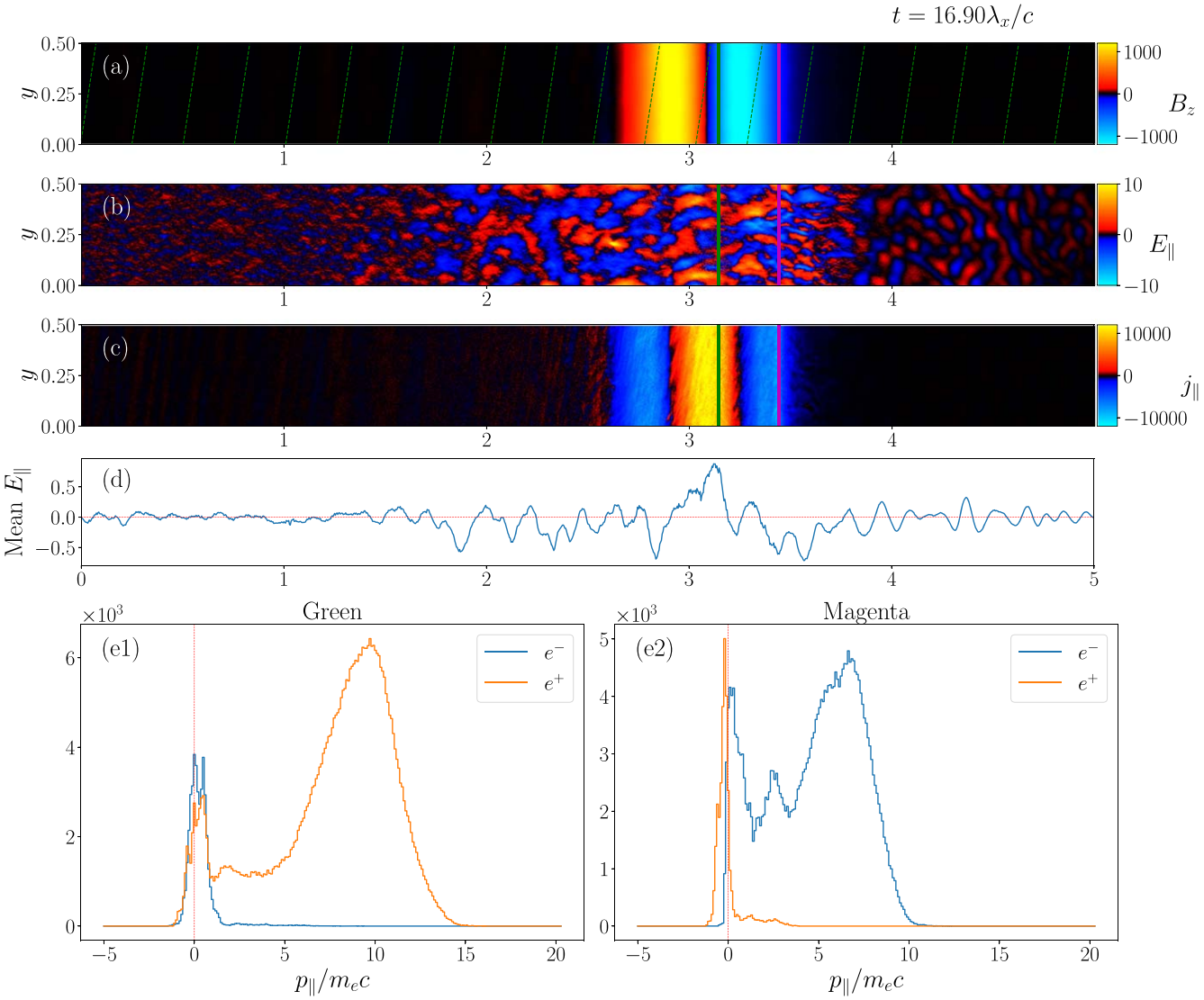

Figure 3. A snapshot of the simulation with $\kappa = 12$. Panels from top to bottom are as follows: (a) the wave magnetic field B_z as color plot and B_0 as dashed green lines; (b) parallel electric field; (c) parallel current density; (d) $E_\parallel$ averaged over y; (e1) momentum distribution of $e^\pm$ in the green region depicted in panels (a)–(c); (e2) momentum distribution of $e^\pm$ in the magenta region in panels (a)–(c). B and E are measured in units of $m_ec^2/e\lambda_x$, while j is measured in units of $m_ec^3/4\pi e\lambda_x^2$.

at the center of the wave profile. In the simulations shown below, we always keep $\sigma_w \sim 100$ so that $\sigma_w \gg \sqrt{\kappa}$. This regime is realistic for Alfvén waves in a neutron star magnetosphere. The simulation results will verify that, in this limit, the amount of wave energy converted to particle kinetic energy is small, and the wave electromagnetic fields remain close to the initial force-free solution.

4.2. Waves in a Uniform Background

We performed a series of simulations where κ is constant in the box. The value of κ varied from 2 to 100 between the different runs. In all of these simulations, we observed the rapid development of the two-stream instability, breaking $E_\parallel$ into Langmuir modes that propagate with the Alfvén wave. The instability saturates quickly, heating the particle streams and leading to a sustained momentum space configuration shown in Figure 3.

This configuration differs from the two-fluid model of Section 3. The plasma momentum distribution in the wave can be described as a relativistic, hot, and charge-separated stream traveling into a quasi-neutral static plasma. This configuration is prone to a warm version of the two-stream instability, exciting electrostatic wave modes that scatter the fast moving particles to lower velocities, creating a *bridge* in momentum space between the relativistic stream and the static plasma (see panel (e) in Figure 3). The bridge particles gradually fall behind the current-carrying beam, which tends to reduce j. As a result, the plasma responds by inducing a small $\langle E_\parallel \rangle$, which keeps accelerating the particles traveling in the wave. Effectively, this creates an anomalous resistivity that continually dissipates the Alfvén wave energy. A small fraction of the dissipated energy is converted into the plasma waves launched into the upstream, but most of the energy goes into gradual acceleration of the relativistic beam.

Figure 4 shows this gradual and continual acceleration of the current conducting particles, as well as the scaling of their Lorentz factor with κ. At any given time, the peak Lorentz factor scales as $\sqrt{\kappa}$ across the simulations with different κ. The acceleration in all cases seems to be consistent with an average

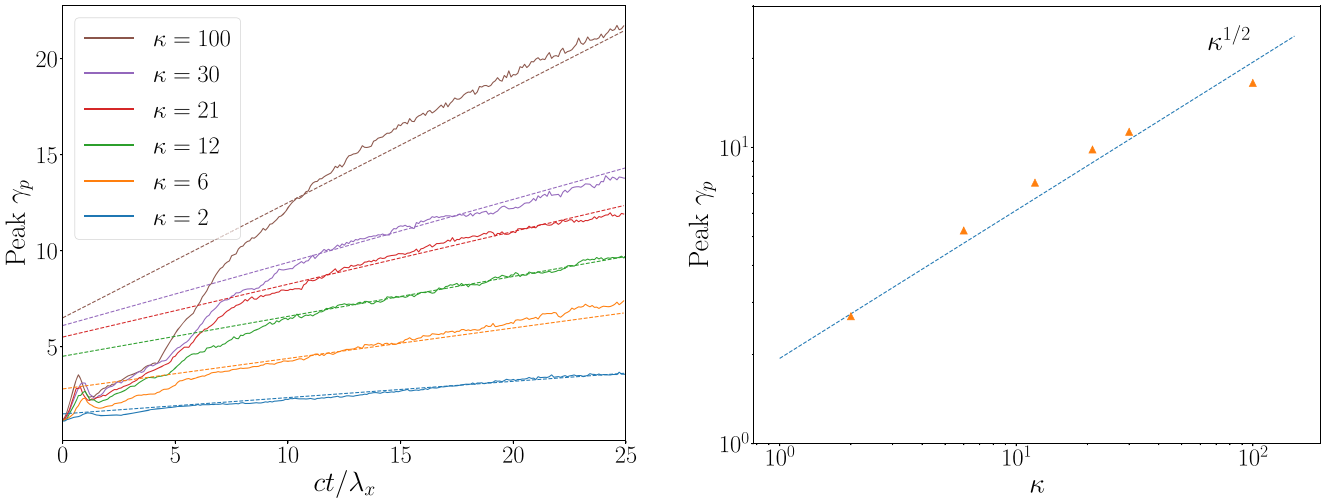

Figure 4. Particle Lorentz factor vs. κ. Left panel: growth of peak Lorentz factor of the current conducting particles in the wave at different κ. Dashed lines have slopes $0.4\sqrt{\kappa}/\lambda$, and are acceleration models with constant $E_\parallel$. Right panel: orange triangles are peak Lorentz factors at $ct/\lambda_x = 15$, while the blue dashed line indicates a simple power law $\gamma_p \propto \kappa^{1/2}$, which is the prediction of the two-fluid toy model.

dissipating electric field

$$\langle E_\parallel \rangle \approx 0.4\sqrt{\kappa}\,\frac{m_e c^2}{e\lambda}, \tag{24}$$

where λ is the full wavelength of the Alfvén wave. This electric field is much smaller than the (nondissipative) spike of $E_\parallel$ that was needed in the two-fluid model to polarize the background plasma. The fractional dissipation rate of the wave energy density U_w can be estimated as

$$\frac{\dot{U}_{\rm diss}}{U_w} \sim \frac{E_\parallel j_{\rm A}}{B_w^2/8\pi} \sim \frac{\sqrt{\kappa}\,c}{\sigma_w \lambda}. \tag{25}$$

Thus, a fraction $\sqrt{\kappa}/\sigma_w$ of the wave energy is dissipated in time λ/c.

In the toy model of Section 3, charges swept by the wave are accelerated to $\gamma \sim \sqrt{\kappa}$, flow with the wave for a *residence time* $t_{\rm res} \sim \gamma^2\lambda/c \sim \kappa\lambda/c$, and exit behind it with the same upstream condition. By contrast, the simulations demonstrate that a dissipative electric field $\langle E_\parallel \rangle$ is induced, which accelerates charges linearly with time well beyond $\sqrt{\kappa}$. The characteristic particle Lorentz factor grows as $\gamma \sim 0.4\sqrt{\kappa}\,ct/\lambda$, and this continued acceleration has an important consequence: it helps the wave to trap the plasma. The residence time $t_{\rm res} \sim \kappa ct^2/\lambda$ grows quadratically with time, and exceeds the elapsed time t at $t \sim \lambda/(\kappa c)$. When $\kappa \gg 1$, $t_{\rm res}$ quickly becomes much greater than t, i.e., the plasma is trapped in the Alfvén wave. As a result, the wave can be supported by the advected plasma for a long time.

After the onset of trapping, we observe that the wave and the advected relativistic plasma go through the low-density background plasma with weak interaction—the $e^\pm$ background remains nearly static inside the wave. This is the origin of the momentum distribution with a hot relativistic beam propagating through the static quasi-neutral plasma in Figure 3. The saturated two-stream instability sustains the dissipative $\langle E_\parallel \rangle$.

The gradual acceleration of the beam $\gamma \propto t$ should saturate if it reaches the group speed of the wave,

$$\frac{v_A}{c} = \sqrt{\frac{\sigma}{1+\sigma}}, \quad \gamma_{\rm A} = \sqrt{1+\sigma}, \tag{26}$$

where $\sigma = B_0^2/4\pi n_w m_e c^2$ is the magnetization parameter, and n_w is the plasma density in the wave, which can significantly exceed the background n_0 in the regime of $\kappa \gg 1$. The acceleration of the plasma beam carried by the wave should saturate when the beam Lorentz factor reaches $\gamma \sim \sqrt{\sigma}$, and further dissipation will likely go into heating the plasma beam. Note, however, that it can take a long time for the wave to reach this saturated regime, and it may not occur in a real neutron star magnetosphere. Instead, the beam speed can become limited by the radiative drag due to the resonant Compton scattering of X-rays around magnetars.

The fractional dissipation rate (Equation (25)) scales with κ and σ_w, and it is independent of the relative amplitude of the Alfvén wave B_w/B_0. We performed a series of simulations with the same B_w and different background magnetic field strengths B_0, such that B_w/B_0 ranges from 0.01 to 0.5. We find that in all cases, as long as B_w and κ remain constant and $\sigma_w \gg \sqrt{\kappa}$, the energy dissipation rates and particle acceleration histories are identical.

Using an approximate volume of the emission region $V_\lambda \sim \lambda\ell_\perp 2\pi r \sin\theta \sim \lambda\ell_\perp 2\pi r (r/r_m)^{1/2}$, one can estimate the dissipation power per wavelength λ,

$$L_{\rm diss} \sim E_\parallel j_{\rm A} V_\lambda \sim \sqrt{\kappa}\,\frac{ceB_w r^{3/2}}{r_e r_m^{1/2}}. \tag{27}$$

Since $B_w = B_w^\star (r/r_*)^{-3/2}$, the dissipation power is essentially only dependent on κ, the initial Alfvén wave amplitude emitted by the star $B_w^\star$, and the maximum extent of the field line r_m.

4.3. Wave Propagation through a Density Jump

The numerical results described in Section 4.2 are applicable to waves propagating with a slowly changing κ. We now investigate the opposite regime where κ increases suddenly, on a length scale that is comparable or shorter than the Alfvén wavelength. In particular, we wish to check whether there is any dramatic transient behavior in the extreme limit when the Alfvén wave propagates across a sharp boundary where κ transitions from <1 to $\gg 1$.

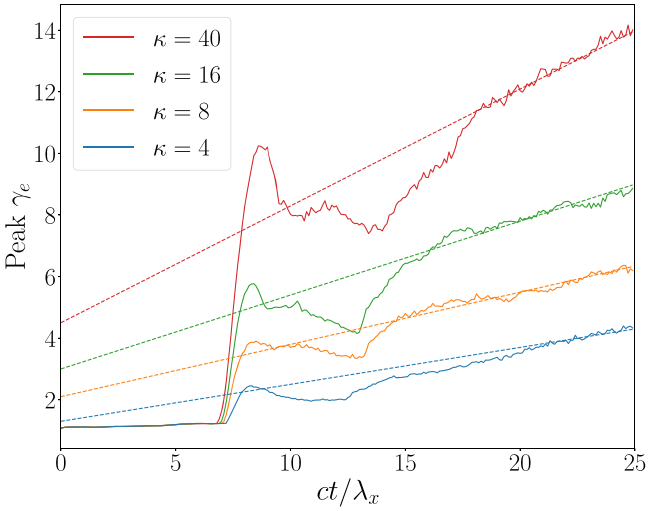

Figure 5. Evolution of maximum electron Lorentz factor vs. κ when there is a density jump. Dashed lines have slopes $0.4\sqrt{\kappa}/\lambda$, and are acceleration models with constant $\langle E_\parallel \rangle$. After the transient when the wave goes across the density jump, particle acceleration proceeds in a similar fashion as Figure 4.

We use the same simulation setup as described in Section 4.2, with the exception that n_0 drops sharply at $x = 0.4L_x$. We have carried out a series of simulations where $\kappa = 0.8$ for $x < 0.4L_x$ and κ for $x > 0.4L_x$ is a constant value above unity. In our simulations, the value of κ after the jump ranges from 4 to 40. Figure 5 shows the evolution of the peak electron Lorentz factors for these runs before and after the density jump.

We find that during its encounter with the density jump, the Alfvén wave induces a coherent $E_\parallel \propto \sqrt{\kappa}/\lambda_x$ to quickly accelerate charges of the right sign to $\gamma \sim \sqrt{\kappa}$. The parallel electric field separates the charges and sweeps the required amount of $e^\pm$ with the wave to conduct the required current. The most significant acceleration happens near the leading edge of the wave, which is negatively charged in our wave profile (see panel (c) of Figure 3). The encounter phase with the high $E_\parallel$ has a short duration, and the total dissipated energy during the simulation is dominated by the later phase, when the wave continues to propagate through the low-density background. At this late phase, the wave behavior is similar to that found in Section 4.2 with $\kappa = \text{const}$.

4.4. Multiple Wavelengths

So far we have studied the plasma dynamics in a charge-starved Alfvén-wave packet of only one wavelength. A realistic starquake will likely excite a train of many wavelengths.

The simplified two-fluid model described in Section 3 extends trivially to multiple wavelengths: the plasma enters and exits each wavelength in exactly the same state with zero $\beta_\pm$; hence each wavelength can be treated independently. However, in the more realistic picture shown by the simulations in Sections 4.2 and 4.3, the plasma becomes trapped and advected by the wave, which could affect the plasma dynamics in subsequent wavelengths. To investigate how charge-starvation occurs for a wave train, we carried out an additional series of simulations with four wavelengths in the Alfvén-wave packet. One of these simulations is shown in Figure 6.

The simulations show that charge-starvation effects first develop in the leading wavelength, where the plasma is accelerated through the mechanism described in Section 4.2 and quickly becomes trapped with the wave. Before the plasma is completely trapped within the wavelength, some charges will leak into the next wavelength, delaying its transition into charge-starvation. Eventually, all wavelengths become charge-separated and enter the advection regime. We find that the particle distributions in the train of multiple wavelengths are identical to that in the single-wavelength simulation shown in Section 4.2. In this regime, the quasi-neutral background plasma flows through each wavelength, slightly heated by the Langmuir oscillations in the wave, but otherwise unaffected by it. Therefore, each wavelength still remains largely independent. We believe that this result is scalable to yet more wavelengths. This can be further tested in the future with larger simulations.

5. Discussion

We have studied the propagation of Alfvén waves in different plasma densities, in particular when the background plasma density is insufficient to support the required current j_A. We find that such *charge-starved* Alfvén waves still manage to propagate with the required current and charge densities by advecting the required charges with it. The wave becomes charge-separated rather than truly charge-starved, and the charge carriers move at near the speed of light. In the highly magnetized regime of $B_w^2/4\pi \gg n_0 m_e c^2$, only a small amount of the Alfvén wave energy needs to be converted to particle kinetic energy to sustain this configuration. The particle acceleration process is gradual and driven by a small regular $\langle E_\parallel \rangle$ averaged over Langmuir oscillations.

We find that the dissipation rate of this electric field scales with $\sqrt{\kappa}$, and estimate the local dissipation rate to be Equation (27). We compare this to the FRBs observed from the galactic magnetar SGR 1935+2154 that is concurrent with an X-ray burst. The energy budget of the X-ray burst is consistent with an Alfvén wave of amplitude $B_w^\star \sim 10^{-3} B_p \sim 10^{11}$ G (Yuan et al. 2020). Assuming a large $\kappa \sim 100$, and that the wave is launched on a field line with maximum extent $r_m \sim 10^2 R_*$, we can then estimate the maximum power dissipated per wavelength λ in the wave entering charge-starvation as

$$L_{\rm diss} \sim 10^{30}\, \kappa^{1/2} \left(\frac{B_w^\star}{10^{11}\,{\rm G}}\right)\left(\frac{r_m}{10^8\,{\rm cm}}\right)^{-1/2} {\rm erg\ s^{-1}}. \quad (28)$$

Assuming that the particles in the wave are accelerated to Lorentz factors of $\gamma \sim \sqrt{\kappa}$, their emission will be beamed into a solid angle $\delta\Omega \sim \gamma^{-2}$, enhancing the apparent luminosity by γ^2. The duration of the emission is governed by the length of the wave train, with no Doppler compression. The resulting observed isotropic equivalent luminosity from one wavelength λ may be estimated as $L \sim 10^{33} (\kappa/100)^{3/2}\,{\rm erg\ s^{-1}}$, if one optimistically assumes a 100% radiative efficiency.

Note that the beaming $\delta\Omega \sim \gamma^{-2}$ occurs only if the radiating particles move along nearly straight magnetic field lines. In reality, the field lines are curved on a length scale not much greater than the wavelength. This broadens the emission solid angle and reduces the effect of Doppler beaming on the apparent luminosity. Thus, the observed luminosity will be even lower than the estimate above. This luminosity can hardly reach the observed luminosity of the FRB from SGR 1935+2154, $L_{\rm radio} \sim 3 \times 10^{37}\,{\rm erg\ s^{-1}}$ (CHIME/FRB Collaboration et al. 2020).

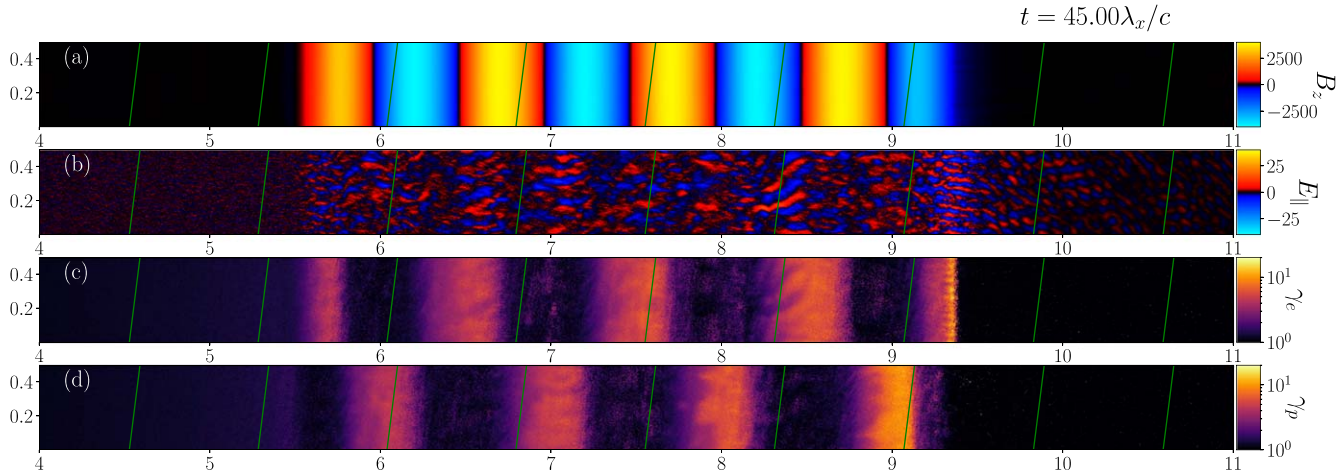

Figure 6. A snapshot of the simulation with $\kappa = 13.5$, showing only a portion of the box. Panels from top to bottom are as follows: (a) the wave magnetic field B_z as color plot and B_0 as dashed green lines; (b) parallel electric field; (c) mean Lorentz factor of electrons; (d) mean Lorentz factor of positrons. The units used are the same as in Figure 3. The wave propagates to the right of the box. The charge-starvation effect is strongest in the leading (rightmost) wavelength of the wave train.

Our simulations do not show strong bunching of $e^{\pm}$ in the saturated plasma oscillations in the Alfvén wave, which would be needed for efficient coherent emission. Even if the plasma did form bunches, the particles do not gain enough energy or sufficiently high Lorentz factors for coherent emission in the radio band. Therefore, our results do not support the proposal that charge-starved Alfvén waves produce FRBs (Lu et al. 2020). The insufficient energy budget becomes particularly severe for cosmological FRBs, whose luminosities reach 10^{42} erg s^{-1}. The mechanism of FRB emission remains a debated topic (Lyubarsky 2021). Even if the radio waves are emitted in the inner magnetosphere, it will be subjected to plasma effects during its propagation, which may significantly change its waveform, or lead to strong scattering (Beloborodov 2021a).

In the vicinity of magnetars, the resonant inverse-Compton scattering of the thermal X-ray photons flowing from the star can exert an efficient drag force on the plasma, depending on the location in the magnetosphere (Beloborodov 2013; Thompson & Kostenko 2020). This can create a significant additional channel for dissipation in the charge-starved Alfvén waves, which can potentially convert most of the energy gained by the particles into hard X-ray emission. The resulting X-ray luminosity may be in the observable range. The inverse-Compton scattering may also induce pair production, which increases the background plasma density and thus reduces κ. These effects will be studied in a future work.

Much stronger dissipation of relativistic Alfvén waves can occur when they collide with each other and create regions of $E > B$ (Li et al. 2021) or form turbulence cascades (Thompson & Blaes 1998; Li et al. 2019). Strong dissipation also occurs if the wave grows to a nonlinear amplitude $B_w > B_0$, triggering magnetic reconnection (Yuan et al. 2020). Strong dissipation generally creates copious $e^{\pm}$ pairs with a subrelativistic temperature, and the released energy is promptly radiated in a hard X-ray burst (Beloborodov 2021b).

We thank Wenbin Lu, Dmitri Uzdensky, and Jens Mahlmann for helpful discussions. We also thank the anonymous referee for suggestions that improved the manuscript. A.C. is supported by NSF grants AST-1806084 and AST-1903335. Y.Y. is supported by a Flatiron Research Fellowship at the Flatiron Institute, Simons Foundation. A.M. B. is supported by NASA grant NNX 17AK37G, NSF grant AST 2009453, Simons Foundation grant #446228, and the Humboldt Foundation. X.L. is supported by the Natural Sciences and Engineering Research Council of Canada (NSERC), funding reference #CITA 490888-16, and the Jeffrey L. Bishop Fellowship. Research at Perimeter Institute is supported in part by the Government of Canada through the Department of Innovation, Science and Economic Development Canada and by the Province of Ontario through the Ministry of Colleges and Universities. This research used resources of the Oak Ridge Leadership Computing Facility at the Oak Ridge National Laboratory, which is supported by the Office of Science of the U.S. Department of Energy under Contract No. DE-AC05-00OR22725.

ORCID iDs

Yajie Yuan https://orcid.org/0000-0002-0108-4774
Andrei M. Beloborodov https://orcid.org/0000-0001-5660-3175
Xinyu Li https://orcid.org/0000-0003-0750-3543

References

Beloborodov, A. M. 2013, ApJ, 777, 114
Beloborodov, A. M. 2021a, ApJL, 922, L7
Beloborodov, A. M. 2021b, ApJ, 921, 92
Blaes, O., Blandford, R., Goldreich, P., & Madau, P. 1989, ApJ, 343, 839
Bochenek, C. D., Ravi, V., Belov, K. V., et al. 2020, Natur, 587, 59
Bransgrove, A., Beloborodov, A. M., & Levin, Y. 2020, ApJ, 897, 173
CHIME/FRB Collaboration, Andersen, B. C., Bandura, K. M., et al. 2020, Natur, 587, 54
Duncan, R. C., & Thompson, C. 1992, ApJL, 392, L9
Goldreich, P., & Julian, W. H. 1969, ApJ, 157, 869
Kumar, P., & Bošnjak, Ž. 2020, MNRAS, 494, 2385
Kumar, P., Lu, W., & Bhattacharya, M. 2017, MNRAS, 468, 2726
Li, X., & Beloborodov, A. M. 2015, ApJ, 815, 25
Li, X., Beloborodov, A. M., & Sironi, L. 2021, ApJ, 915, 101
Li, X., Zrake, J., & Beloborodov, A. M. 2019, ApJ, 881, 13
Lu, W., Kumar, P., & Zhang, B. 2020, MNRAS, 498, 1397
Lyubarsky, Y. 2021, Univ, 7, 56
Melrose, D. B. 1986, Instabilities in Space and Laboratory Plasmas (Cambridge: Cambridge Univ. Press)
Mereghetti, S., Savchenko, V., Ferrigno, C., et al. 2020, ApJL, 898, L29
Palfreyman, J., Dickey, J. M., Hotan, A., Ellingsen, S., & van Straten, W. 2018, Natur, 556, 219
Ruderman, M. 1976, ApJ, 203, 213

Swisdak, M. 2006, arXiv:physics/0606044
Thompson, C., & Blaes, O. 1998, PhRvD, 57, 3219
Thompson, C., & Kostenko, A. 2020, ApJ, 904, 184
Yuan, Y., Beloborodov, A. M., Chen, A. Y., & Levin, Y. 2020, ApJL, 900, L21